3D cell morphology detection by association for embryo heart morphogenesis

Rituparna Sarkar, Daniel Darby, Sigolène Meilhac, Jean-Christophe Olivo-Marin

3D cell morphology detection by association for embryo heart morphogenesis

Rituparna Sarkar[1,4] ![ORCID], Daniel Darby[2,3], Sigolène Meilhac[2,3] and Jean-Christophe Olivo-Marin[1,4,*] ![ORCID]

[1]BioImage Analysis Unit, Institut Pasteur, Paris, France
[2]Unit of Heart Morphogenesis, Imagine-Institut Pasteur, Paris, France
[3]Université de Paris, INSERM UMR 1163, Paris, France
[4]CNRS UMR 3691, Paris, France
*Corresponding author. E-mail: jean-christophe.olivo-marin@pasteur.fr

Abstract

Advances in tissue engineering for cardiac regenerative medicine require cellular-level understanding of the mechanism of cardiac muscle growth during embryonic developmental stage. Computational methods to automatize cell segmentation in 3D and deliver accurate, quantitative morphology of cardiomyocytes, are imperative to provide insight into cell behavior underlying cardiac tissue growth. Detecting individual cells from volumetric images of dense tissue, poised with low signal-to-noise ratio and severe intensity in homogeneity, is a challenging task. In this article, we develop a robust segmentation tool capable of extracting cellular morphological parameters from 3D multifluorescence images of murine heart, captured via light-sheet microscopy. The proposed pipeline incorporates a neural network for 2D detection of nuclei and cell membranes. A graph-based global association employs the 2D nuclei detections to reconstruct 3D nuclei. A novel optimization embedding the network flow algorithm in an alternating direction method of multipliers is proposed to solve the global object association problem. The associated 3D nuclei serve as the initialization of an active mesh model to obtain the 3D segmentation of individual myocardial cells. The efficiency of our method over the state-of-the-art methods is observed via various qualitative and quantitative evaluation.

Impact Statement

This article discusses a 3D cell segmentation method for detecting individual cells from light-sheet volumetric images of cardiac tissue of murine embryo. Automatized 3D segmentation is a crucial step to deliver accurate, quantitative descriptions of cell morphology in 3D—relevant to the study of cell structure underlying cardiac muscle growth during development, with potential applications in tissue engineering for cardiac regenerative medicine. The article has been jointly written by development biologists with expertise in the quantitative analysis of heart development, and computer scientists with expertise in the development of mathematical models for image and data analysis. This collaboration makes this research an authentic endeavor to develop impactful tools and knowledge relevant to the biology of the cardiac muscle.

1. Introduction

Recent works have shown coordinated cell division during the embryonic stage[1–3] regulates the orientation of myofibres and consequently determines heart contraction patterns. Studying morphogenesis of a developing heart is thus crucial to accelerate fundamental research in cardiology. Novel imaging techniques, such as light-sheet microscopy have allowed larger depth of field imaging, facilitating cellular level 3D imaging of murine embryo heart. The quantification of cellular morphology in 3D is, however, restricted by the availability of dedicated automatic computational methods. In this article, we propose a method to segment cells from 3D light-sheet microscopy images of murine myocardial tissue (with membrane and nuclei fluorescence) to facilitate precise extraction of morphological features of cardiomyocytes.

While light-sheet microscopy allows larger depth of field imaging, this introduces greater inference from dense tissue leading to significant intensity heterogeneity. This adds to the challenges in identification of individual cells (segmentation) from dense tissue samples imaged in 3D. The tissue characteristics of the imaging organ/organism introduce significant signal variation and structural alteration. In comparison to the more commonly used prototype organisms—*zebrafish* or *Caenorhabditis elegans*, lower transparency of mouse myocardial tissue leads to low signal to noise ratio. Additionally, the myocardial tissue, unlike the epithelial, has more irregular architecture as shown in Figure 1. Due to this nonuniform structure of myocardium in the heart, regions consisting of nonmyocardial cells (shown in Figure 1 with blue arrows) are introduced in the images. It is necessary to identify and discard these regions at an early computational stage for a robust morphogenesis analysis of cardiomyocytes.

1.1. Related works

In the literature, few works have proposed methods for cell segmentation from 3D tissue samples. The more commonly used approaches[4–8] employ only cell membrane images (without nuclei staining). These methods mainly employ techniques for cell membrane image enhancement and subsequent detection of the intermembranous regions to identify individual cells. The efficiency of these methods relies mainly on 3D membrane enhancement to deal with the intensity in-homogeneity and incomplete structures. Various techniques, such as Hessian-based image enhancement[4,7], unsupervised clustering,[5] and supervised machine learning[8] have been adopted in literature to obtain a noise-free prediction of the cell membrane. The enhanced images of cell membrane are then subject to 3D Watershed[4–8] to achieve final cell segmentation. A slightly different approach is proposed in Ref. (9), where watershed segmentation is first employed to detect cells from enhanced 2D membrane images. The detected cellular regions are then merged axially based on various constraints to obtain final 3D cell reconstructions. Using solely the cell membrane for segmentation is intuitive only when nuclei information is unavailable. But as pointed out in Ref. (4), these approaches do not allow to discriminate between cellular and noncellular regions. This leads to significant false positives in more complex and developed tissue, such as the myocardium.
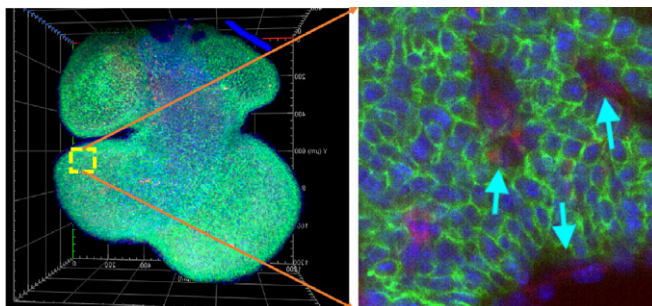
Figure 1. *View of an entire mouse embryo heart (left) and enlarged view of a cropped portion (right). The green and blue channels correspond to cardiomyocyte membranes and nuclei, respectively. Epicardial and endocardial cells without membrane staining are marked by blue arrows.*

In presence of both membrane and nuclei images, the nuclei information can aid in determining precise cell locations. Very few works in literature[10,11] have employed multifluorescence images, cell membrane and nuclei, to guide cell segmentation. Azuma and Onami[10] achieve this by using detected nuclei regions as the seed for watershed method to segment cells from *C. elegans* embryo images. The nuclei segmentation is performed using the difference of Gaussian filtering. This approach relies heavily on the correct choice of parameters and is inadequate in spatially resolving nuclei from low-resolution 3D images. An alternative approach was developed by Pop *et al.*[11], where the intensity clustering technique was employed for 3D nuclei detection from confocal microscopy images of murine heart. This was followed by coupled active mesh initialized at the detected nuclei and evolved using the membrane cues to obtain 3D cell segmentation. The 3D active mesh approach is robust to noisy and discontinuous membrane structure avoiding leakage in the cell membrane. However, the clustering approach is dependent on image intensity and tends to over-segment nuclei due to the intensity heterogeneity. Neither of these methods combines the nuclei and membrane information to aid in their detection and for the final cell segmentation.

In order to deal with the aforementioned challenges and shortcomings of state-of-art methods in 3D cell segmentation from tissues, we propose a method that exploits the robustness of convolutional neural network for detection, efficiency of a graph-based association method, and active mesh to obtain 3D reconstruction of cardiomyocytes *Ca3D*.

1.2. Main contributions

In this article, we propose a novel approach to 3D cell segmentation from multifluorescence image of cardiac tissue of a mouse embryo. A single convolutional neural network is designed to first obtain nuclei and membrane detection from 2D slices of a 3D volumetric image. The neural network is designed to disregard nuclei from nonmyocardial regions at an initial computational stage. The 3D nuclei reconstruction is then obtained via solving an optimization problem, which associates detected 2D nuclei along the axial direction. This global nuclei association approach aids in delineating cells along axial direction while maintaining a more regular 3D structure. A linear optimization embedded in an alternating direction method of multipliers is designed to solve the association problem. The global association problem can easily employ biologically inspired constraints within the optimization framework. Further, this also eliminates nuisances of over-detection due to intensity heterogeneity as observed in clustering[11] and local heuristics-based approaches[9]. Finally, an active mesh initialized at the detected 3D nuclei is evolved using cell membrane-based force function to segment individual cells from the cluttered environment. The overview of the proposed method is shown in Figure 2. The main highlights of the article are summarized as follows:
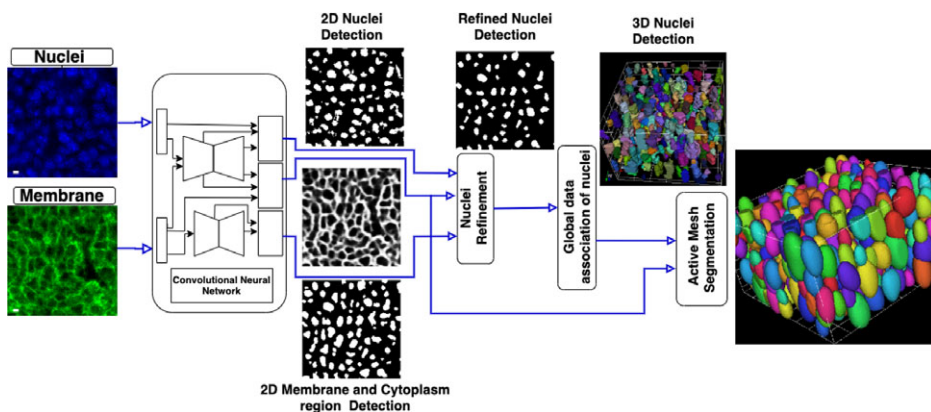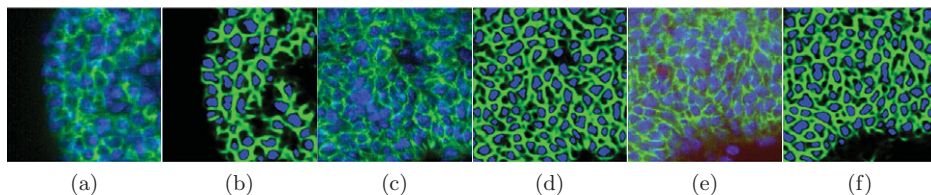

Figure 2. *Overview of Ca3D cell segmentation method.*

Figure 3. *Deep learning results of 2D detection of membrane (green) and nuclei (blue) (from three different ventricular regions) are shown in (b,d,f). The corresponding original images are shown in (a,c,e).*

– A hybrid pipeline that exploits a multitask neural network (mutually benefit from the multichannel signal) for 2D detection and an optimization method to reconstruct 3D nuclei from 2D detections. The final cell segmentation is obtained by employing an active contour model initialized at the 3D nuclei detections and evolved using the membrane information.

– The optimization problem is designed to associate 2D nuclei along axial direction to obtain 3D nuclei reconstruction. The global association problem is formulated as a linear optimization problem with quadratic cost and biologically inspired cost function.

– A novel algorithm is designed which embeds the linear optimization in an alternating direction method of multipliers to solve the association problem.

The article is organized as follows. In Section 2, the detailed pipeline developed for 3D cell segmentation is described. In Section 3, we describe in detail the mathematical formulation for obtaining 3D reconstruction from 2D detection. In Section 4, we provide the extensive experimental evaluation and comparison with existing methods for 3D cell segmentation. Finally, we conclude the article discussing the advantages of our method and future directions.

2. Ca3D: Pipeline for 3D Segmentation of Cardiomyocytes

The proposed hybrid method exploits convolutional neural networks and classical image processing approaches to obtain robust cell segmentation from 3D images of tissue. The different steps of this pipeline are described in detail in the following subsections.

2.1. Multitask learning for membrane and nuclei detection

The membrane cue is invariably necessary to segment cells from immuno-fluorescent images[4,7–10] but as discussed in Ref. (10) combining the nuclei and membrane is more conducive for cell segmentation from tissue samples. This is specifically more relevant for cardiomyocyte segmentation which demonstrates significant variation in cell morphology and noncellular structures. In the convolutional neural network community, the efficacy of multitask learning has been demonstrated in the literature[12,13], for various image analysis applications. We exploit the multitask neural network approach to combine the membrane and nuclei information at an initial detection stage for more robust detection.

The neural network is trained on 2D slices of nuclei and membrane images. The network is designed with a partially shared encoder between the nuclei and membrane channels to mutually benefit from one another. Further, due to low resolution, spatially delineating two nuclei is a challenging task. In this scenario, the membrane cue is advantageous to spatially resolve nuclei. An additional constraint for a robust delineation of the nuclei is employed via detection of intermembranous (inverted membrane signal) regions, which would ideally denote the cytoplasmic regions of the myocardial cells. An initial convolution block encodes the features from nuclei and membrane, which are then concatenated and input to the common encoder. Two separate decoder-blocks input the original features and output from the encoder to provide pixel-wise prediction of the nuclei and membrane region. The cytoplasmic region
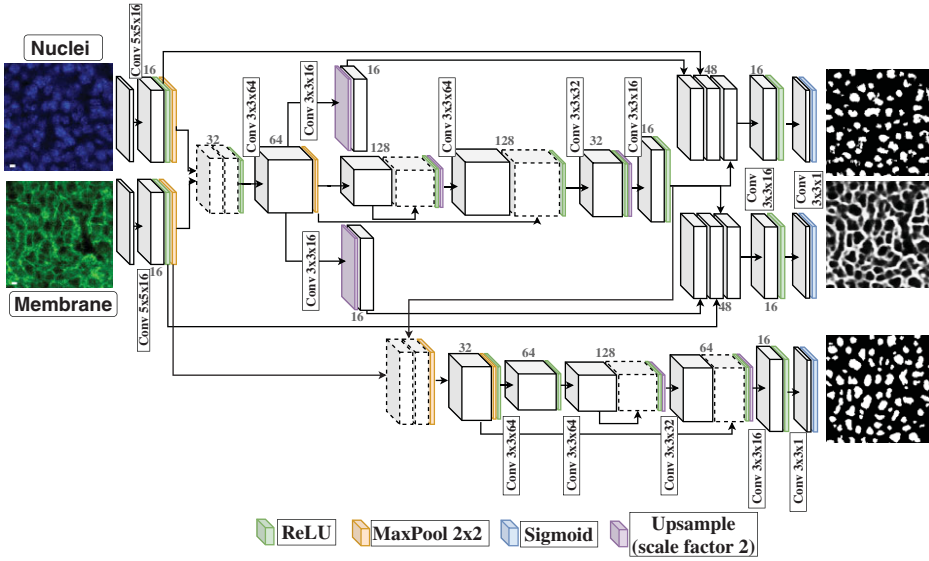
Figure 4. *Proposed neural network architecture is shown in the figure. The size of convolution kernel and the channel (height × width × channel size) for each layer are shown in the above figure. The channel size in each layer is also marked above each block in the diagram.*

detection is performed via another branch which uses input from the membrane features and nuclei-membrane encoder output. The detailed network architecture is shown in Figure 4. The neural network is trained on the combined loss function from the three channels,

$$L_m\left(I_m, \widehat{I}_m\right) + L_d\left(\left(I_{im}\right), \left(\widehat{I}_{im}\right)\right) + L_d\left(I_n, \widehat{I}_n\right). \tag{1}$$

Here I_m, I_n are the ground truth for membrane and nuclei, whereas $\widehat{I}_m$, $\widehat{I}_n$ are the corresponding predictions. I_{im} is the intermembranous regions denoted by $(1 - I_m)$, which is precomputed and augmented (nonmyocardial regions are removed) during the ground truth generation process.

Dice loss L_d is used for nuclei and inverted membrane detection whereas mean squared loss, L_m is used for membrane detection. The final refined 2D nuclei prediction is obtained as an overlap of nuclei and intermembranous region prediction. This aids in discarding the nonmyocardial cell nuclei and noisy detection. Sample prediction results of the nuclei and membrane are shown in Figure 3. As can be seen, the enhanced membrane signal and the desired nuclei are obtained with significantly good precision.

2.2. 3D nuclei detection via association

The 3D nuclei structure can be obtained from the 2D detections. This can be achieved by associating the 2D detections axially to construct the 3D nuclei. A naïve approach is to employ local heuristics (such as position, size, etc.)[9,14] to solve the association problem, but often lead to irregular and erroneous 3D structures. In Refs. (15–17), the authors present more sophisticated formulations for 3D segmentation by association. Xu *et al.*[17] employ a graph-based global association to associate 2D detections for 3D neuron segmentation. In Ref. (15), Mukherjee *et al.* used a graph-based method which solves the minimum spanning tree problem to associate disjoint objects and achieve 3D neuron segmentation. An attraction force-based association of disjoint objects in 3D is designed by Ref. (16). These aforementioned methods[15,16,18] have been designed for segmenting neurons, which demonstrate a tubular tree-like geometry unlike cell nuclei that are more convex in structure. A robust data association for 3D nuclei segmentation forms the core of our method since this serves as the initialization of an active mesh model for 3D cell segmentation. Here, we design a novel graph-based association approach to detect 3D nuclei

while maintaining the convex geometry and certain biological constraints. In this section, we formally define the mathematical formulation of the association problem.

Let $\mathcal{I}$ be the 3D volumetric image of nuclei and $\mathcal{I}_z$ be a 2D image (zth slice of the volumetric image $\mathcal{I}$) in the domain $[0,1]$. Let $\Phi = \left\{ o_z^j \right\}_{z=1\ldots N_s, \, j=1\ldots n_z}$ a set consisting of binary object on 2D images and $o_z^j \cap o_z^k = \varnothing$, where $j, k \in \{1 \ldots n_z\}$. Here, N_s denotes the number of 2D slices and n_z denotes the number of 2D objects in zth slice. $\Psi = \left\{ \psi_p \right\}_{p=1\ldots N_3}$, where N_3 is the total number of 3D objects in the volumetric image $\mathcal{I}$ and $\psi_p \cap \psi_q = \varnothing$. For 3D nuclei detection, we seek to find a function $\mathcal{F} : \Phi \mapsto \Psi$. The mapping, $\mathcal{F}$, is accomplished by solving a constrained optimization problem, which simultaneously selects a 2D object and a link connecting two 2D objects from consecutive z-slices. The problem is defined as follows:

$$\min_{Y_{i,j}} \sum_{i,j} \left\{ C_{i,j} \, Y_{i,j} + C_{s,i} \, Y_{s,i} + C_{t,i} \, Y_{t,i} + C_i \, Y_i + \sum_k Q_{i,j,k} \, Y_{i,j} \, Y_{j,k} \right\} \tag{2}$$
$$s.t. \sum_{i,j \in \varepsilon} Y_{i,j} = \sum_{j,k \in \varepsilon} Y_{j,k}; \; Y_{i,j} \in \{0,1\} \; Y_i \in \{0,1\}.$$

Here a graph structure is imposed on the ensemble of 2D detections. Each 2D nuclei detection o_z^i is considered as a node x_i in the graph (Figure 5a). The connectivity between nodes is defined such that x_i in stack z is connected to a node x_j in the subsequent stack $z+1$. Each node in the graph is connected to a source, s and a sink, t. The edge between two nodes x_i and x_j is denoted by an indicator function $Y_{i,j}$, that is, $Y_{i,j} = 1$ if an edge is present between two 2D objects and 0 otherwise. $Y_{i,j}$ determines the connectivity between 2D detections to reconstruct the 3D nuclei. The nucleus connectivity is penalized by a weight $C_{i,j}$, which is computed based on how likely $\mathcal{F}\left(o_z^i\right) = \mathcal{F}\left(o_{z+1}^j\right)$. The link between a source and a node is denoted by $Y_{s,i}$ and $Y_{i,t}$ with connectivity weights $C_{s,i}$ and $C_{i,t}$ respectively. C_i is defined as the likelihood of a 2D object belonging to any flow path. The second order cost $Q_{i,j,k}$ employed in the optimization regulates if nuclei from three subsequent stacks belong to the same 3D object. The optimal solution is obtained by sending the maximum flow from source to sink while minimizing overall cost. The 2D objects in one flow path from source to sink can be inferred as one 3D object. A detailed description of the optimization problem solution is given in Section 3.

This optimization problem satisfies three main properties necessary to reconstruct 3D nuclei from 2D detection.

Property 1. $\mathcal{F}\left(o_z^j\right) \neq \mathcal{F}\left(o_z^k\right)_{k \neq j}$. This property implies that two disjoint objects in a particular 2D imaged plane, belong to two different 3D objects. It is satisfied directly during the graph construction where no edge is present between detection (nodes) in the same plane.

(a) (b)
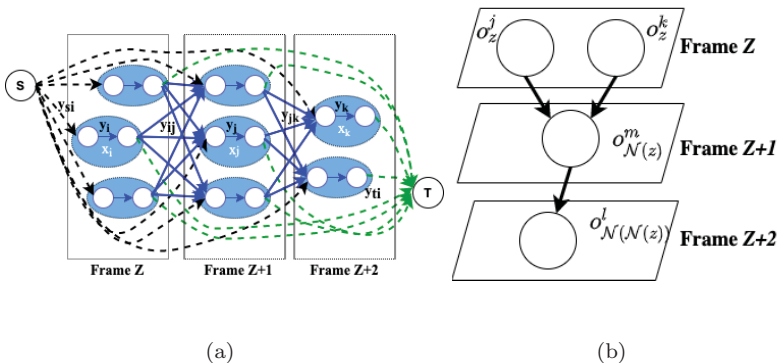
Figure 5. *The schematic for the directed graph connecting the nuclei is shown in (a). Subfigure (b) shows a schematic for the possible conflicts which need to be handled in the mathematical formulation.*

Property 2. The second property implies that one 2D object in a particular z-slice can be connected to only one 2D object in the subsequent z-slice, that is, If $o_z^j \cap o_{\mathcal{N}_z}^m \neq \varnothing$ and $o_z^k \cap o_{\mathcal{N}_z}^m \neq \varnothing$, where $j \in \{1 \dots n_z\}$ and $m \in \{1 \dots n_{\mathcal{N}_z}\}$, (as shown in *Figure 5b*), then either one of the following needs to be satisfied:

a. $\mathcal{F}\left(o_z^j\right) = \mathcal{F}\left(o_{\mathcal{N}_z}^m\right) \neq \mathcal{F}\left(o_z^k\right),$
b. $\mathcal{F}\left(o_z^j\right) \neq \mathcal{F}\left(o_{\mathcal{N}_z}^m\right) = \mathcal{F}\left(o_z^k\right),$
c. $\mathcal{F}\left(o_z^j\right) \neq \mathcal{F}\left(o_{\mathcal{N}_z}^m\right) \neq \mathcal{F}\left(o_z^k\right).$

Here $\mathcal{N}_z$ denotes the neighboring 2D slice. The constraint $\sum_{i,j \in \varepsilon} Y_{i,j} = \sum_{j,k \in \varepsilon} Y_{j,k}$ in equation (2) is essential in satisfying this property. The constraint indicates that the number of incoming edges to a node equals the number of outgoing edges. When the total number of incoming edges equals one it satisfies the property that a 2D detection can be connected to only one 2D detection in the subsequent stack.

Property 3. The third property takes into consideration how objects from three subsequent slices can be mapped to the same 3D object. If $o_i^j \cap o_{\mathcal{N}_z}^m \cap o_{\mathcal{N}(\mathcal{N}_z)^1} \neq \varnothing$ and $o_z^k \cap o_{\mathcal{N}_z}^m \cap o_{\mathcal{N}(\mathcal{N}_z)}^l \neq \varnothing$ (as in *Figure 5b*, where $l \in \{1 \dots n_{\mathcal{N}(\mathcal{N}_z)}\}$, then either of the following needs to be satisfied:

a. $\mathcal{F}\left(o_z^j\right) = \mathcal{F}\left(o_{\mathcal{N}_z}^m\right) = \mathcal{F}\left(o_{\mathcal{N}(\mathcal{N}_z)}^l\right) \neq \mathcal{F}\left(o_z^k\right),$

b. $\mathcal{F}\left(o_z^j\right) = \mathcal{F}\left(o_{\mathcal{N}_z}^m\right) \neq \mathcal{F}\left(o_{\mathcal{N}(\mathcal{N}_z)}^l\right) \neq \mathcal{F}\left(o_z^k\right),$

c. $\mathcal{F}\left(o_z^j\right) \neq \mathcal{F}\left(o_{\mathcal{N}_z}^m\right) = \mathcal{F}\left(o_{\mathcal{N}(\mathcal{N}_z)}^l\right) = \mathcal{F}\left(o_z^k\right),$

d. $\mathcal{F}\left(o_z^j\right) \neq \mathcal{F}\left(o_{\mathcal{N}_z}^m\right) = \mathcal{F}\left(o_{\mathcal{N}(\mathcal{N}_z)}^l\right) \neq \mathcal{F}\left(o_z^k\right),$

e. $\mathcal{F}\left(o_z^j\right) \neq \mathcal{F}\left(o_{\mathcal{N}_z}^m\right) \neq \mathcal{F}\left(o_{\mathcal{N}(\mathcal{N}_z)}^l\right) \neq \mathcal{F}\left(o_z^k\right),$

f. $\mathcal{F}\left(o_z^k\right) = \mathcal{F}\left(o_{\mathcal{N}_z}^m\right) \neq \mathcal{F}\left(o_{\mathcal{N}(\mathcal{N}_z)}^l\right) \neq \mathcal{F}\left(o_z^j\right).$

The second-order cost, $Q_{i,j,k}$ determines when $Y_{i,j} = 1$ and $Y_{j,k} = 1$ simultaneously and thus x_i, x_j, and x_k of stacks z, $z + 1$, and $z + 2$ belong to the same 3D object. The optimization details to solve for $\mathcal{F}$ using equation (2) are detailed in Section 3.

2.3. Active mesh cell segmentation

The 3D nuclei detection provides an approximate location of nuclei. In order to obtain final cell segmentation, the membrane information is essential. Edge-based deformable models[11,19] are more appropriate choice for segmentation in this scenario. This is specifically advantageous in our case, since this formulation allows the mesh to coincide with image edge features and simultaneously forbid overlapping of meshes[19]. The active mesh model implemented in the bioimage analysis software Icy[20] is used for this purpose. The active contour evolution parameters are estimated in an automated manner as described in Refs. (11) and (19). We initialize the active mesh at the detected nuclei and evolve using the 3D membrane image $\mathcal{I}_M$. Each 2D slice in $\mathcal{I}_M$ is multitask neural network membrane prediction $\tilde{I}_m$.

3. Mathematical Framework

The solution of global data association problem, without the second-order constraint, can be achieved via constrained linear programming[21] or network flow algorithm[22,23]. The sparse matrix $\mathbf{Q}$ imposing the higher-order connectivity constraint on the graph makes the optimization problem nontrivial. We propose a relaxed linearization technique of the quadratic objective function via variable substitution, which can

then be solved via network flow algorithm embedded within an alternating direction method of multipliers framework[24].

The objective function in the proposed optimization problem equation (2) can be written in a matrix form as

$$\min_{\mathbf{Y}} \mathbf{C}^T \mathbf{Y} + \mathbf{Y}^T \mathbf{Q} \mathbf{Y}$$

$$s.t. \sum_{i,j \in \varepsilon} Y_{i,j} = \sum_{j,k \in \varepsilon} Y_{j,k}; \ Y_{i,j}, \ Y_i \in \{0,1\}. \tag{3}$$

Here $\mathbf{C}, \mathbf{Y} \in \mathcal{R}^N$ and $\mathbf{Q} \in \mathcal{R}^{N \times N}$, N denotes the number of edges in the graph.

The relaxed linearization of the objective function in equation (3) via variable substitution is then written as

$$\min_{\mathbf{Y},\mathbf{Z}} \mathbf{C}^T \mathbf{Y} + \mathbf{Z}^T \mathbf{Q} \mathbf{Y}$$

$$s.t. \sum_{i,j \in \varepsilon} Y_{i,j} = \sum_{j,k \in \varepsilon} Y_{j,k}; \ Y_{i,j} \in \{0,1\} \ Y_i \in \{0,1\} \tag{4}$$

$$\mathbf{Y}^T = \mathbf{Z}^T; Z_{i,j} \geq 0; Z_{i,j} - 1 = 0.$$

It should be noted here, that $\mathbf{Y}$ is a binary integer, but imposing similar constraints on variable $\mathbf{Z}$ would require to solve dual linear integer programming problem. In order to avoid that, we impose the designed constraints on the relaxation variable $\mathbf{Z}$. In addition to equality constraint with binary variable $\mathbf{Y}$, $\mathbf{Z}$ should have a nonnegative structure. The imposed constraints on $\mathbf{Z}$ imply that it will be as close to zero as possible when $\mathbf{Y} = 0$ and $\mathbf{Z} \simeq 1$ when $\mathbf{Y} = 1$.

We employ alternating direction method of multipliers to solve the augmented Lagrangian formulation of the problem defined in equation (4). The inequality constrained can be handled by introducing a slack variable v such that $Z - v = 0$. The augmented Lagrangian of is then given as

$$\mathbf{C}^T \mathbf{Y} + \mathbf{Z}^T \mathbf{Q} \mathbf{Y} + f(v) + \lambda_1 |\mathbf{Z} - \mathbf{Y}| + \lambda_2 |\mathbf{Z} - \mathbf{1}| + \lambda_3 |\mathbf{Z} - v| + \frac{\mu}{2} \left(\|\mathbf{Z} - \mathbf{Y}\|^2 + \|\mathbf{Z} - \mathbf{1}\|^2 + \|\mathbf{Z} - v\|^2 \right). \tag{5}$$

Here $f(v) = max(0, \lambda_3 + \mu \mathbf{Z})$. λ_1, λ_2, and λ_3 are the Lagrangian multiplier and μ is the penalty parameter of the augmented Lagrangian function.

The variable $\mathbf{Z}$, $\mathbf{Y}$, λ_1, λ_2 and λ_3 are updated in an alternating minimization fashion. The solution to obtain $\mathbf{Z}$ and $\mathbf{Y}$ are explained as follows.

3.1. Update Z

The solution for $\mathbf{Z}$ can be obtained by first taking the derivative of the augmented Lagrangian with respect to $\mathbf{Z}$ and setting it to zero. The derivative of cost function in equation (5) with respect to Z is given as

$$\min_{\mathbf{Z}} \mathbf{Z}^T \mathbf{Q} \mathbf{Y} + \lambda_1 |\mathbf{Z} - \mathbf{Y}| + \lambda_2 |\mathbf{Z} - \mathbf{1}| + \lambda_3 |\mathbf{Z} - v| + \frac{\mu}{2} \left(\|\mathbf{Z} - \mathbf{1}\|^2 + \|\mathbf{Z} - \mathbf{Y}\|^2 + \|\mathbf{Z} - v\|^2 \right). \tag{6}$$

By setting the derivative of equation (6) to 0 and setting $\beta = \frac{1}{3\mu}$, we obtain a closed-form solution of $\mathbf{Z}$ as

$$\mathbf{Z} = \beta((\mu - \mathbf{Q})\mathbf{Y} + \mu(1 + v) - \lambda_1 - \lambda_2 - \lambda_3). \tag{7}$$

3.2. Update Y

The solution for $\mathbf{Y}$ is obtained by solving the augmented Lagrangian with the constraints on $\mathbf{Y}$ as in equation (3):

$$\min_{\mathbf{Y}} \mathbf{C}^T \mathbf{Y} + \mathbf{Z}^T \mathbf{Q} \mathbf{Y} + \lambda_1 |\mathbf{Z} - \mathbf{Y}| + \frac{\mu}{2} \|\mathbf{Z} - \mathbf{Y}\|^2$$

$$s.t. \sum_{i,j \in \varepsilon} Y_{i,j} = \sum_{j,k \in \varepsilon} Y_{j,k}; \ Y_{i,j} \in \{0,1\}; \ Y_i \in \{0,1\}. \tag{8}$$

Since $Y_{i,j}$ is a binary variable, one can assume $Y_{i,j}^2 = Y_{i,j}$. We can then rewrite $\|Z_{i,j} - Y_{i,j}\|_2^2 = Y_{i,j} - 2Y_{i,j}Z_{i,j} + Z_{i,j}^2$. By imposing this approximation[25], $\|\mathbf{Z} - \mathbf{Y}\|^2 \simeq (1 - 2\mathbf{Z})^T\mathbf{Y} + \|\mathbf{Z}\|^2$. The optimization problem for $\mathbf{Y}$ can now be written as

$$
\min_{\mathbf{Y}} \left(\mathbf{C}^T + \mathbf{Z}^T\mathbf{Q} - \lambda_1 + \mu(1 - 2\mathbf{Z})^T\right)\mathbf{Y}
$$
$$
s.t. \sum_{i,j \in \varepsilon} Y_{i,j} = \sum_{j,k \in \varepsilon} Y_{j,k}; \; Y_{i,j} \in \{0,1\}; \; Y_i \in \{0,1\}.
$$
(9)

The optimal flow $\mathbf{Y}$, is obtained by solving equation (9) as a min-cost network flow optimization using the push-relabel algorithm[22,23]. The pseudo-algorithm of the optimization problem is given in Algorithm 1.

Algorithm 1 Ca3D

Input: $C_{i,j}$, $Q_{i,j,k} \forall i,j \in 1\dots N$
Output: $Y_{i,j} \forall i,j \in 1\dots N$
Method: The ADMM update for the Augmented Lagrangian is as follows:
Initialize $\mathbf{Y}^\tau$ by solving **equation (2)** without the second-order cost
For $\tau \geq 0$; For $t \geq 0$,

$$
\mathbf{Z}^{t+1} = \beta\left((\mu - \mathbf{Q})\mathbf{Y}^\tau + \mu(1 + v) - \lambda_1^t - \lambda_2^t - \lambda_3^t\right), \tag{10}
$$
$$
\lambda_1^{t+1} = \lambda_1^t + \mu\left(\mathbf{Z}^{t+1} - \mathbf{Y}^k\right), \tag{11}
$$
$$
\lambda_2^{t+1} = \lambda_2^t + \mu\left(\mathbf{Z}^{t+1} - 1\right), \tag{12}
$$
$$
\lambda_3^{t+1} = \lambda_3^t + \mu\left(\mathbf{Z}^{t+1} - v^t\right), \tag{13}
$$
$$
v^{t+1} = \max\left(0, \lambda_3 + \mu\mathbf{Z}^{t+1}\right). \tag{14}
$$

Update $\mathbf{Y}^{\tau+1}$ using **equation (9)** with $\mathbf{Z}^{t+1}, \lambda_1^{t+1}$.

3.3. Graph weight selection

In addition to formulating the optimization method, a robust design of the link costs is an important aspect of the data association problem. For our problem, the link cost connecting the 2D nuclei detections o_z^i and o_{z+1}^j is designed taking into account three different criteria: spatial distance between 2D objects, the change in nuclei size, and a biologically inspired membrane-overlap condition. The spatial distance is simply obtained as the Euclidean distance between two nuclei given as $c_{ij}^c = \frac{\|c(o_z^i) - c(o_{z+1}^j)\|_2^2}{2\sigma_c^2}$, where $c(o_z^i)$ is the centroid of nuclei o_z^i and σ_c constrains the spatial distance (axially) between two nuclei centers. The size constraint is imposed by the change in area of two nuclei given by $c_{ij}^a = \frac{\|a(o_z^i) - a(o_{z+1}^j)\|_2^2}{2\sigma_a^2}$, $a(o_z^i)$ is the area of nuclei detection o_z^i and σ_a^2 controls the allowed change in the area. This criterion imposes that a significant increase (or decrease) in 2D nuclei detection size denote they are part of different 3D objects, that is, $\mathcal{F}(o_z^i) \neq \mathcal{F}(o_{z+1}^j)$ (or false positives in 2D detection).

The biologically inspired membrane-overlap criterion states that even if o_z^i and o_{z+1}^j are spatially close, $\mathcal{F}(o_z^i) \neq \mathcal{F}(o_{z+1}^j)$, if cell membrane is present between them. We ensure this criterion by designing a membrane cross-over cost defined by,

$$
c_{ij}^m = \frac{1}{N} \sum_{k = p(i,j)-\frac{N}{2}}^{p(i,j)+\frac{N}{2}} e^{-\frac{(k - p(i,j))^2}{2\sigma_m^2}} f(M_{k,z}, M_{k,z+1})). \tag{15}
$$

Here $f(M_{.,z}, M_{.,z+1})$ is the interpolation of membrane stack between z and $z + 1$. N is the number of pixels within the window centered at $p(.)$. $p(i,j)$ is the mid-point of the line joining centroids of nuclei o_z^i and o_{z+1}^j. The cost of linking two nuclei, $C_{i,j}$ is given as the sum of c_{ij}^c, c_{ij}^a, and c_{ij}^m. The pairwise cost, $Q_{i,j,k}$ is formulated as the sum of $C_{i,j}$ and $C_{j,k}$ to ensure the co-occurrence of three nodes in a single flow. This
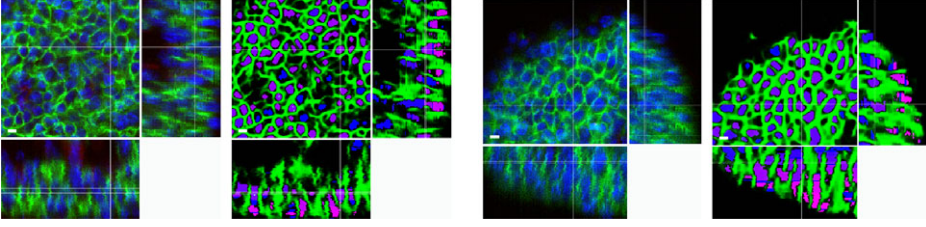
Figure 6. *Nuclei association results. First and third column shows the original images. Second and fourth column shows nuclei association results (magenta) overlaid on neural network detection of the membrane (green) and nuclei (blue).*

implies that when the link costs concur with the above criteria for three subsequent nuclei o_z^i, o_{z+1}^j, and o_{z+1}^k, then $\mathcal{F}\left(o_z^i\right) = \mathcal{F}\left(o_{z+1}^j\right) = \mathcal{F}\left(o_{z+2}^k\right)$. This also ensures a local smoothness in the linked path.

Sample data association results for 3D nuclei reconstruction are shown in Figure 6. It can be observed from the figure, the nuclei association (overlaid on neural network detection results, in magenta) can delineate nuclei axially even in scenarios where visually identifying the separation is challenging.

4. Experimental Results

Ca3d is applied to segment individual cells from 3D images of murine heart from light-sheet microscopy images. The experimental details and the results are discussed in the following subsections.

4.1. Data description

The mouse hearts were dissected from embryos at 10.5 days after fertilization (E10.5). They were fixed in 4% paraformaldehyde and labeled as a whole mount by immuno-staining with anti-Scrib and anti-Cadh2 antibodies to detect cardiomyocyte membranes. Nuclei were counter-stained with Hoechst. Whole-mount hearts were cleared with CUBIC approach[26] and mounted on 0.4% agarose in Reagent-2 in a capillary. Multichannel 8-bit images were acquired on a Z.1 (Zeiss) light-sheet microscope with a 20×/1.0 objective with voxel resolution is $0.63 \times 0.63 \times 1.26$ μm.

4.2. Neural network training

We obtain 56—2D cropped images (dimension 255×255) from the 3D scan of an embryo ventricular region. They are manually annotated to create nuclei and membrane ground truth. The 2D ground truth was generated in a semi-automated manner using Icy, a bio-image analysis software[20]. Ground truth for nuclei was generated by drawing manual contours. The membrane images are first enhanced using a hessian enhancement scheme and manual thresholding to obtain binary detection. An in-painting tool[20] is used to connect (disconnect) membrane regions to preserve continuity (remove noisy structures) of the structures. Finally, we compute the inverse of membrane ground truth and apply area-threshold to discard nonmyocardial regions. This forms the ground truth for the intermembrane prediction branch. We perform a qualitative and quantitative comparison with four state-of-the-art methods to demonstrate the efficacy of our method. A dataset consisting of 500 images is created by employing various augmentations, such as horizontal and vertical flips, rotation, variation in brightness.

The neural network is trained for 100 epochs with a learning rate of 10^{-3} and a learning rate decay of 0.9 at every 50 epochs. Adam Optimizer[27] is used to train the network. Details of the network architecture are shown in Figure 4. The filter dimensions (height and width) and the number of channels (Channel Size) at each convolution layer are shown in the aforementioned figure (above each convolution step). The channel size at each step is also marked above each block in the schematic. The dotted blocks denote the concatenation of channels. Each convolution layer consists of ReLU activation followed by

Maxpool (size 2×2) for the encoder section and an upsampling (scale factor 2) in the decoder section. Sigmoid activation layer is used in the final convolutional layer to obtain a smooth and scaled output.

4.3. 3D segmentation and validation

3D segmentation using *Ca3d* pipeline is performed on six crops of size $255 \times 255 \times 70$, extracted from the ventricular region of the volumetric image of two different embryos. From each crop, the 2D slices of nuclei and membrane channel are first used to obtain 2D nuclei, membrane and intermembranous segmentation using the multitask neural network. As discussed earlier, the final refined 2D nuclei prediction is obtained as an overlap of nuclei and intermembranous region predictions. The 3D nuclei detections are obtained via the proposed association approach. Before applying active contour, the 3D nuclei of relatively small size are identified and discarded. This ensures errors due to nuclei over-segmentation are reduced in the final step. Due to the size and shape variations (resulting from intensity inhomogeneity), the terminal regions of 3D nuclei (axially) may lead to multiple associated fragments causing nuclei over-segmentation. As we seek to employ a single nuclei detection during active contour initialization for individual cell segmentation, we employ, a simple morphology-based threshold approach to discard relatively smaller 3D nuclei. Only the associated 3D nuclei which consist of 2D detections comprising of seven or more Z-slices are used for active contour segmentation. This is determined from expert annotation of nuclei. 2D nuclei regions (from neural network) of the cardiomyo-cytes are merged along the axial direction manually by a developmental biologist to obtain 3D nuclei structures (this is also used to compute semi-manual 3D cell segmentation for validation as discussed later in Section 4.4). From these annotations, minimum size (elongation) of the nuclei was determined as 12 µm. With Z-resolution 1.26 µm and keeping into account possible errors ensuing from neural network and the 3D association, 9 µm(1.26×7 µm) is selected as threshold of nuclei size. 3D nuclei objects below this size are discarded before employing active contour segmentation. This confirms smaller fragments, specifically resulting from over-segmentation of nuclei, are discarded before active contour initialization.

Due to the lack of ground truth in 3D, we first perform manual validation on a part of the segmented data. The segmentation result on the rest of the data is statistically compared with the validation for different cell morphological parameters. We also compare our method with state-of-the-art methods both qualitatively and quantitatively. The details of the validation and comparison methods are given in the following subsections.

4.4. Comparison with competing methods

4.4.1. Comparison methods

We compare *Ca3d* with four competing state-of- the-art methods for cell segmentation from 3D images of tissue. The comparison methods were developed to segment cells from 3D images of confocal or light-sheet microscopy images for different organisms (such as mouse, *C. elegans*) and different developing organs (embryo, heart, and kidney).

   i. Pop *et al.*[11]: The method was developed for cell segmentation from 3D images of mouse heart from confocal microscopy. This method employs a hierarchical *K*-means clustering[18,28] for 3D nuclei detection. The active surface model[19] is then initialized at the detected nuclei and evolved using the enhanced membrane image.
  ii. *RACE*[9]: An automated method was designed for cell segmentation of developing embryos from light-sheet and confocal microscopy images. The method employs membrane enhancement techniques to detect intermembranous regions indicating the cellular cytoplasmic region. Mor-phological operations are employed to enhance and discard detected regions of irrelevant size. 2D watershed segmentation is employed to segment cellular regions in each Z-stack, which are then merged using heuristics to obtain the 3D cell reconstruction.

   iii. *3DMMS*[4]: The method employs 3D hessian-based membrane enhancement and intermembrane information for cell region detection. 3D watershed segmentation is performed using these detected regions and a distance computed using the inverted membrane. In this method, pre-computed nuclei lineage details from 3D image sequences are used to improve the final segmentation. Due to the absence of nuclei lineage information for our experimentation protocol, we employ the nuclei predicted using the neural network for postprocessing.

   iv. *ShapeMetrics*[8] This method performs cell membrane detection using *Ilastik*[29], an interactive machine learning approach for object prediction. Different threshold values are then applied for binary segmentation of the membrane and the threshold value producing visually best prediction is selected. 3D watershed segmentation on the enhanced membrane detection is performed to obtain cell segmentation.

4.4.2. 3D segmentation validation

As we have mentioned earlier, obtaining ground truth for individual cells from the tissue is a time consuming and laborious task even for experts in the field. Consequently, we compare the cell morphological values with two types of validation methods—manual and semi-manual cell segmentation.

   i. *Manual evaluation*: The manual evaluation was performed by looking at individually segmented cells and original images by experts to determine the segmentation quality. The segmentation accuracy was measured based on two different criteria: (a) cell-overlap: axially and spatially nonoverlapping cells and (b) approximate cell size. The nonoverlapping criterion considers if the segmentation contour overlaps multiple cells either axially or spatially. The cell size criterion looks at the number of *Z*-slices comprising a cell and cell elongation. Each of the segmented cells is given a high-confidence or low confidence score based on the above two criteria. Manual evaluation is performed on randomly selected 300 cells for three different volumetric crops. The frequency distribution of the evaluated cells based on high-confidence value using cell size and cell overlap criterion are individually provided in Figure 7. The distribution of the cell morphological parameters, when both criteria have high confidence value simultaneously, is also shown in Figure 7 (in green). Although the distributions are almost similar to individual criteria, high confidence in both provides a more precise range for cell parameters. We employ this combined high-confidence range to evaluate the efficiency of *Ca3D* and compare it with state-of-the-art methods.

   ii. *Semi-manual 3D cell segmentation*: A semi-manual method is used to generate cell segmentation for comparison and evaluation. In this process, the 2D nuclei detection (from neural network) of the cardiomyocytes are merged along the axial direction manually by a developmental biologist. The shape and size change of detected nuclei, spatial displacement, presence of cell membrane are evaluated manually during the merging procedure. The merged nuclei act as the initialization of active meshes which is evolved using the detected membrane image are to reconstruct individual cells in 3D. This also provides a confidence measure for the 3D nuclei reconstruction problem[30].
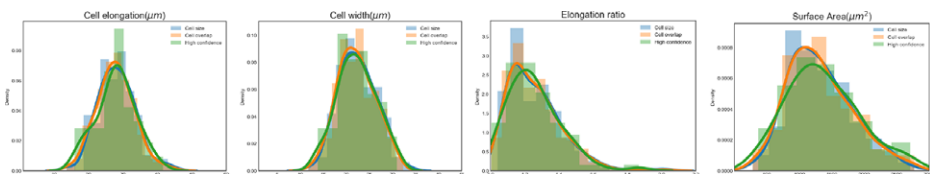
Figure 7. *The distribution of cells within a valid range for each cell morphological parameter using different validation criteria.*

4.4.3. Quantitative comparison with cell morphology distribution profile

The methods are compared with the above manual and semi-manual validation techniques with respect to various cell morphological parameters: the cell elongation, cell-width, cell elongation ratio, surface area of cells. Any one of these cell parameters is not sufficient to assess the efficacy of a method, but if the performance is uniform over the different parameters, the efficacy is then definitely convincing. The mean and standard deviation of the parameters of segmented cells using *Ca3D*, RACE[9], 3DMMS[4], Shape-Metrics[8], and Pop *et al.*[11] are presented in Table 1. In addition to that, the percentage of over- and undersegmented cells are also presented in Table 1.

It is observed that for different cell parameters, Ca3D performs evenly in comparison to the other methods. For cell elongation, although the mean value of 3DMMS and ShapeMetrics is closer to the manually validated value, a significantly high standard deviation is observed. The mean values for RACE are significantly higher and that of Pop *et al.* are lower compared to the validation data. This observation is also apparent from the distribution of cells in Figure 8a. The distribution of cell population pertaining to cell elongation parameter for Ca3D is comparable to the validation data in comparison to the other methods. A similar observation is made for cell width. While Ca3D and 3DMMS have similar mean values of cell width, 3DMMS demonstrates a higher standard deviation. Pop *et al.* and RACE on the other hand have significantly smaller population mean demonstrating a shift in the cell population density from that of the validation data (Figure 8b). The combined effect of the cell elongation and cell width is reflected in the cell elongation ratio (=cell elongation/cell width). The high cell elongation and low cell width lead to a high value of cell elongation ratio for RACE leading to a more flat distribution (Figure 8c). In comparison, Ca3D demonstrates a distribution, which is concurrent with the validation data and closely followed by Pop *et al.* But, Pop *et al.* demonstrate a lower cell population mean for surface area. Contrarily, 3DMMS has a similar population mean as the validation data but a high standard deviation leading to higher over-sized and under-sized segmented cells.

To quantify the distribution presented in Figure 8b, we compute the KL divergence measure and Bhattacharya distance between the parameter distribution of each comparison method and that of the validation methods. A lower value of the distance measure implies that the distribution is similar. It is noted from Table 1, that Ca3D, for all the cell parameters concur with that of manual validation (7th and 8th column) as well as semi-automatic validation (9th and 10th column).

The percentage of oversegmented, undersegmented, and within-range cells are also presented in Table 1. The range for accurate cell size based on the aforementioned parameters is given as $\mu_v \pm k_v \times \sigma_v$. Here, μ_v and σ_v are the mean and standard deviation of the validated cells. k_v is decided such that 90% of the validated cells are within this range. It is observed, with Ca3D we obtain highest percentages of cells, which lie within the valid range for three of the cell parameters. The number of cells within the correct range for surface area is highest for RACE[9], but percentage of under-sized cells with respect to cell width is comparatively higher, which implies that detected cells are thinner and longer in structure. This is also evident from the elongation ratio values, where RACE[9] demonstrates the highest percentage of over-sized cells. Lowest percentage of over-sized cells is obtained with Pop *et al.*[11], but percentage of undersized cells is significantly high. This is pertaining to the fact that intensity-based clustering possibly detects fragments of nuclei leading to the detection of smaller-sized cells. 3DMMS[4] and ShapeMetrics[8] both demonstrate significantly high percentages of both over-sized and under-sized cells in comparison to Ca3D.

The qualitative evaluation by visual inspection is shown in Figures 9 and 10. The 3D segmented image viewed from three viewing planes is presented in Figure 9. As observed from the images, RACE[9], Pop *et al.*[11], and ShapeMetrics[8] demonstrate significant erroneous cell segmentation involving partial detection, significantly low number of detected cells, ambiguous cell boundary. Cell segmentation obtained using 3DMMS[4] identifies cell which aligns with the cell-membrane but generates over-segmented cells spatially as well as axially. 3D visualization of cell segmentation on a sample volumetric image and 3D images of some individual cells obtained for each of these methods are shown in Figure 10. Significantly, nonconvex and noisy cell-boundary is observed for ShapeMetrics[8], 3DMMS[4], and RACE[9]. Pop *et al.*[11] exhibit a smoother cell boundary owing to the application of active mesh model.

Table 1. *Percentage of over and under segmentation of cells based on cell morphological parameters based on high-confidence validated cells.*

Cell parameters Mean ± SD (Manual Validated) (Semi-Auto Validation)	Method	Mean ± SD (Methods)	Over-sized cells (%)	Under-sized cells (%)	Accurate sized cells (%)	Dist (Manual Valid.)		Dist (Semi-Auto Valid.)	
						KL Div.	Bhatt. Dist.	KL Div.	Bhatt. Dist.
Cell elongation (μm) 27.9 ± 5.6 24.4 ± 5.1	Ca3D	25.2 ± 6.5	3.5	11.7	84.7	0.19	0.04	0.08	0.01
	Pop *et al.*[11]	21.1 ± 8.0	2.5	34.4	63.0	1.21	0.19	0.38	0.08
	RACE[9]	32.9 ± 13.1	5.7	27.3	66.9	0.58	0.10	1.17	0.15
	DMMS[4]	26.9 ± 13.7	15.6	24.9	59.4	1.03	0.17	0.72	0.11
	ShapeMetric[8]	26.9 ± 14.9	17.2	25.0	57.7	2.91	0.41	1.45	0.31
Cell width (μm) 22.3 ± 4.1 17.9 ± 4.5	Ca3D	19.7 ± 4.8	2.9	16.9	80.1	0.43	0.06	0.05	0.01
	Pop *et al.*[11]	16.6 ± 6.8	1.3	40.1	58.5	1.66	0.24	0.30	0.05
	RACE[9]	17.9 ± 7.9	4.1	39.7	56.1	1.48	0.21	0.17	0.03
	DMMS[4]	19.1 ± 8.2	9.9	33.7	56.3	1.54	0.20	0.46	0.07
	ShapeMetric[8]	26.5 ± 14,2	8.7	37.4	53.8	3.10	0.45	2.41	0.29
Elongation ratio 1.25 ± 0.15 1.39 ± 0.2	Ca3D	1.28 ± 0.18	8.8	0.0	91.1	0.04	0.01	0.14	0.03
	Pop *et al.*[11]	1.29 ± 0.29	11.4	0.0	88.5	0.48	0.08	0.43	0.07
	RACE[9]	2.01 ± 0.97	69.1	0.0	30.9	0.11	0.01	0.23	0.05
	DMMS[4]	1.45 ± 0.63	26.8	0.0	73.1	2.33	0.43	1.62	0.25
	ShapeMetric[8]	1.63 ± 1.17	35.6	0.0	64.3	0.69	0.11	0.53	0.09
Surface area (μm²) 1,365.9 ± 549.3 1,262.7 ± 560.6	Ca3D	1,157.9 ± 532.3	3.1	2.9	93.8	0.13	0.03	0.06	0.02
	Pop *et al.*[11]	935.2 ± 574.1	1.5	17.4	80.7	0.36	0.09	0.23	0.06
	RACE[9]	990.2 ± 335.2	0.0	0.0	99.1	0.37	0.09	0.26	0.06
	DMMS[4]	1,402.6 ± 1,338.1	15.9	16.8	67.23	0.70	0.12	0.39	0.08
	ShapeMetric[8]	1,733.6 ± 276.1	17.7	22.0	66.2	0.27	0.06	0.17	0.04
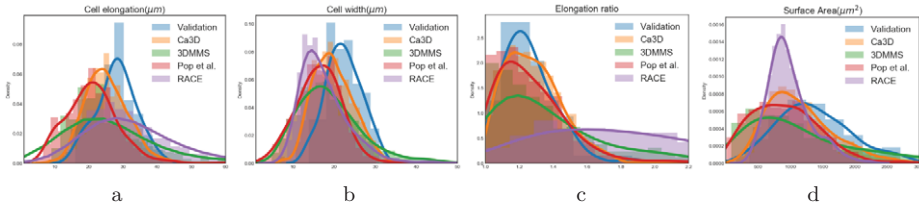
Figure 8. *The distribution of the cells within a valid range for different cell morphological parameter-(a.) cell elongation, (b.) cell width, (c.) elongation ratio and (d.) surface area are shown in this figure.*

a. Original   b. Ca3D   c. Pop et al. [21]   d. RACE [26]   e. 3DMMS [3]   f. Shapemetrics [27]
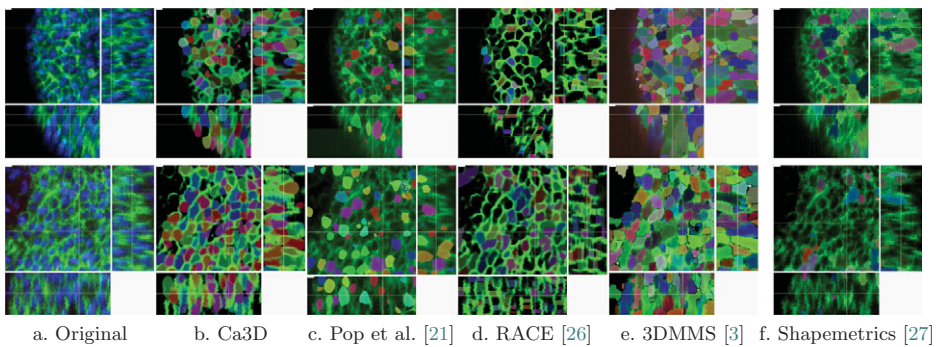
Figure 9. *3D visualization of segmented cells in planar view for two sample crops extracted from ventricular and interventricular regions. The original raw images are shown in (a.) The segmentation method for Ca3D (in b.) and state-of-the-art methods (c.) PoP et al.[18], (d.) RACE[9], (e.) 3DMMS[4], and (f.) ShapeMetrics[8] are shown for visual comparison.*

a. Ca3D   b. Pop et al. [21]   c. RACE [26]   d. 3DMMS [3]   e. Shapemetrics [27]
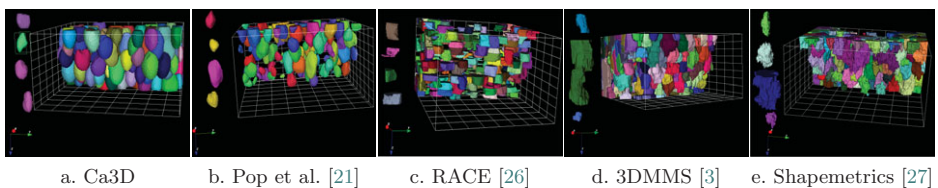
Figure 10. *3D visualization of segmented cells sample crops extracted from ventricular. Sample segmented cells are shown on the left side of each crop. The segmentation method for Ca3D (in b.) and state-of-the-art methods (b.) PoP et al.[18], (c.) RACE[9], (d.) 3DMMS[4], and (e.) ShapeMetrics[8] are shown for visual comparison.*

The superiority in segmentation quality of Ca3D is observed from both Figures 9 and 10 where segmented cells are compact-sized, with smoother boundary complying with the cell membrane while maintaining approximately convex shape.

4.5. Ablation study

We also present a comparison for ablation study for the convolutional neural network. The multitask neural network has three different task (nuclei, membrane, and intermembranous region) detection objectives. The ablation study is performed by using different task combinations to train the neural network. We employ three different tasks combinations: (a) nuclei, (b) nuclei and membrane, and

Table 2. *Ablation study: % of over and under segmentation of cells based on cell morphological parameters and 90% of high-confidence validated cells for different training of the neural network.*

Cell parameter (Mean ± SD [Validated cells])	Method	Mean ± SD (Methods)	Under-size (%)	Over-size (%)
Cell elongation(μm) (27.9 ± 5.6)	Ca3D	25.2 ± 6.5	3.5	11.7
	Nuclei	23.1 ± 8.5	4.5	28.9
	Nuc + Mem	20.6 ± 5.2	0.0	31.1
	Nuc + Inv mem	23.0 ± 11.8	3.3	24
Cell width (μm) (22.3 ± 4.1)	Ca3D	19.7 ± 4.8	2.9	16.9
	Nuclei	17.1 ± 6.4	3.8	38.4
	Nuc + Mem	15.1 ± 4.3	0.7	52.5
	Nuc + Inv mem	18.1 ± 4.69	2.1	48.2
Elongation ratio (1.25 ± 0.15)	Ca3D	1.28 ± 0.18	8.8	0.0
	Nuclei	1.36 ± 0.2	24.5	0.0
	Nuc + Mem	1.38 ± 0.18	23.06	0.0
	Nuc + Inv mem	1.27 ± 0.45	9.2	0.0

(c) nuclei and inverted membrane. For the first and third task combination, we use 3D enhanced membrane (as in Pop *et al.*) for the active contour evolution. Table 2 provides the mean and standard deviation values along with percentage of over- and under-sized cells obtained for each of the neural network task combinations with respect to the validation data. For cell elongation and cell width, a lower percentage of over-sized cells is obtained using nuclei and membrane tasks but demonstrates a higher percentage of under-sized cells. The same setting also demonstrates a high percentage of over-sized cells pertaining to ell-elongation ratio. The error possibly occurs due to the consideration of nonmyocardial cells which are discarded by Ca3D using the combination of nuclei and inverted-membrane function. It is observed from the table, that under different cell parameters, Ca3D demonstrates a higher percentage of correctly sized cells in comparison to the three other task settings of the neural network.

5. Conclusion

In this article, we propose an approach for 3D cell segmentation multifluorescence volumetric images of mouse embryo heart imaged via light-sheet microscopy. We developed a hybrid approach, which exploits the robustness of convolutional neural network, a graph-based association method, and active mesh to delineate individual cells in myocardial tissue. The data association problem, which forms the main backbone of the method is obtained using a novel optimization technique that solves the min-cost network flow problem embedded in an alternating direction method of multipliers framework. We demonstrate the efficacy and superiority of our method via various qualitative and quantitative analyses and comparison with state-of-the-art methods. The experimental validation of our 3D cell segmentation approach provides confidence for the applicability of this method in future analysis of coordinated cell division and cardiac muscle orientation.

Data Availability Statement. The code is available at https://github.com/rituparnaS/3D-cell-segmentation-via-neural-network-and-data-association.

References

1. Economou AD, Brock LJ, Cobourne MT & Green JB (2013) Whole population cell analysis of a landmark-rich mammalian epithelium reveals multiple elongation mechanisms. *Development* **140**(23), 4740–4750.
2. Le Garrec J-F, Ragni CV, Pop S, *et al.* (2013) Quantitative analysis of polarity in 3D reveals local cell coordination in the embryonic mouse heart. *Development* **140**(2), 395–404.
3. Li J, Miao L, Shieh D, *et al.* (2016) Single-cell lineage tracing reveals that oriented cell division contributes to trabecular morphogenesis and regional specification. *Cell Rep* **15**(1), 158–170.
4. Cao J, Wong M-K, Zhao Z & Yan H (2019) 3dmms: robust 3d membrane morphological segmentation of *C. elegans* embryo. *BMC Bioinform* **20**(1), 176.
5. Cao J, Zhao Z & Yan H (2018) Accurate cell segmentation based on biological morphology features. In *2018 IEEE International Conference on Systems, Man, and Cybernetics (SMC)*, pp. 3380–3383. Miyazaki: IEEE.
6. Fernandez R, Das P, Mirabet V, *et al.* (2010) Imaging plant growth in 4d: robust tissue reconstruction and lineaging at cell resolution. *Nat Methods* **7**(7), 547.
7. Mosaliganti KR, Noche RR, Xiong F, Swinburne IA & Megason SG (2012) Acme: automated cell morphology extractor for comprehensive reconstruction of cell membranes. *PLoS Computat Biol* **8**(12), e1002780.
8. Takko H, Pajanoja C, Kurtzeborn K, Hsin J, Kuure S & Kerosuo L (2020) Shapemetrics: a userfriendly pipeline for 3d cell segmentation and spatial tissue analysis. *Dev Biol* **462**, 7–19.
9. Stegmaier J, Amat F, Lemon WC, *et al.* (2016) Real-time three-dimensional cell segmentation in large-scale microscopy data of developing embryos. *Dev Cell* **36**(2), 225–240.
10. Azuma Y & Onami S (2017) Biologically constrained optimization based cell membrane segmentation in *C. elegans* embryos. *BMC Bioinform* **18**(1), 307.
11. Pop S, Dufour AC, Le Garrec J-F, *et al.* (2013) Extracting 3D cell parameters from dense tissue environments: application to the development of the mouse heart. *Bioinformatics* **29**(6), 772–779.
12. Ramesh N & Tasdizen T (2018) Cell segmentation using a similarity interface with a multi-task convolutional neural network. *IEEE J Biomed Health Inform* **23**(4), 1457–1468.
13. Sarkar R, Mukherjee S, Labruyère E & Olivo-Marin J-C (2021) Learning to segment clustered amoeboid cells from brightfield microscopy via multi-task learning with adaptive weight selection. In *2020 25th International Conference on Pattern Recognition (ICPR)*, pp. 3845–3852. Milan: IEEE.
14. Wang J, Sarkar R, Aziz A, Vaccari A, Gahlmann A & Acton ST (2017) Bact-3d: a level set segmentation approach for dense multi-layered 3D bacterial biofilms. In *2017 IEEE International Conference on Image Processing (ICIP)*, pp. 330–334. Beijing: IEEE.
15. Mukherjee S, Basu S, Condron B & Acton ST (2013) Tree2tree2: neuron tracing in 3D. In *2013 IEEE 10th International Symposium on Biomedical Imaging*, pp. 448–451. San Francisco, CA: IEEE.
16. Mukherjee S, Condron B & Acton ST (2014) Tubularity flow field - a technique for automatic neuron segmentation. *IEEE Trans Image Process* **24**(1), 374–389.
17. Xu K, Su H, Zhu J, Guan J-S. & Zhang B (2016) Neuron segmentation based on cnn with semi-supervised regularization. In *Proceedings of the IEEE Conference on Computer Vision and Pattern Recognition Workshops*, pp. 20–28. Las Vegas, NV: IEEE.
18. Pop S, Dufour A, Le Garrec J-F, *et al.* (2011) A fast and automated framework for extraction of nuclei from cluttered 3D images in fluorescence microscopy. In *2011 IEEE International Symposium on Biomedical Imaging: From Nano to Macro*, pp. 2113–2116. Chicago, IL: IEEE.
19. Dufour A, Thibeaux R, Labruyere E, Guillen N & Olivo-Marin J-C (2010) 3-d active meshes: fast discrete deformable models for cell tracking in 3-d time-lapse microscopy. *IEEE Trans Image Process* **20**(7), 1925–1937.
20. De Chaumont F, Dallongeville S, Chenouard N, *et al.* (2012) Icy: an open bioimage informatics platform for extended reproducible research. *Nat Methods* **9**(7), 690.
21. Chenouard N, Bloch I & Olivo-Marin J-C (2013) Multiple hypothesis tracking for cluttered biological image sequences. *IEEE Trans Pattern Anal Mach Intell* **35**(11), 2736–3750.

22. Goldberg AV & Tarjan RE (1990) Finding minimum-cost circulations by successive approximation. *Math Oper Res* **15**(3), 430–466.

23. Zhang L, Li Y & Nevatia R (2008) Global data association for multi-object tracking using network flows. In *2008 IEEE Conference on Computer Vision and Pattern Recognition*, pp. 1–8. Anchorage, AK: IEEE.

24. Boyd S, Parikh N & Chu E (2011) *Distributed Optimization and Statistical Learning via the Alternating Direction Method of Multipliers*. Delft: Now Publishers.

25. Chari V, Lacoste-Julien S, Laptev I & Sivic J (2015) On pairwise costs for network flow multi-object tracking. In *Proceedings of the IEEE Conference on Computer Vision and Pattern Recognition*, pp. 5537–5545. Boston, MA: IEEE.

26. Le Garrec J-F, Domnguez JN, Desgrange A, *et al.* (2017) A predictive model of asymmetric morphogenesis from 3D reconstructions of mouse heart looping dynamics. *elife* **6**, e28951.

27. Kingma DP & Ba J (2014) Adam: a method for stochastic optimization. *arXiv preprint arXiv:1412.6980*.

28. Dufour A, Meas-Yedid V, Grassart A & Olivo-Marin J-C (2008) Automated quantification of cell endocytosis using active contours and wavelets. In *2008 19th International Conference on Pattern Recognition*, pp. 1–4. Tampa, FL: IEEE.

29. Sommer C, Straehle C, Koethe U & Hamprecht FA (2011) Ilastik: interactive learning and segmentation toolkit. In *2011 IEEE International Symposium on Biomedical Imaging: From Nano to Macro*, pp. 230–233. Chicago, IL: IEEE.

30. Sarkar R, Darby D, Foucambert H, Meilhac S & Olivo-Marin J-C (2021) Nu3d: 3D nuclei segmentation from light-sheet microscopy images of the embryonic heart. In *2021 IEEE 18th International Symposium on Biomedical Imaging (ISBI)*, pp. 929–933. Nice: IEEE.